processes

MDPI

Article

Pore-Scale Experimental Investigation of the Residual Oil Formation in Carbonate Sample from the Middle East

Yongjie Liu, Jian Pi and Kaijun Tong *

CNOOC International Limited, Beijing 100028, China; yiyuqingcheng614@163.com (Y.L.); pijian@cnooc.com.cn (J.P.)
* Correspondence: tongkj@cnooc.com.cn

Abstract: Select porous carbonate cores are used to carry out water-flooding oil micro-CT flooding experiments, and use image processing to separate oil, water, microfacies, and rock skeleton. The gray value is used to determine the distribution position of the microfacies sub-resolution remaining oil. The gray image resolution is improved by the SRCNN method to improve the pore identification accuracy. The distribution and evolution law of the sub-resolution remaining oil after the displacement is determined by the oil-water distribution results. Using the SRCNN method, the pore recognition accuracy of the original scanned images of the two samples was increased by 47.88 times and 9.09 times, respectively. The sub-resolution residual oil and the macro-pore residual oil were determined from the CT scan images after the brine was saturated and divided into five categories. With the increase in the displacement ratio, the columnar and droplet residual oil of the low-permeability samples first increased and then decreased, and the cluster residual oil gradually decreased. The continuous residual oil of the hypertonic samples gradually decreased, and the discontinuous residual oil gradually increased. According to the research results of carbonate pore throat identification and sub-resolution microscopic residual oil change characteristics after water flooding under the SRCNN method, a method for distinguishing porous carbonate reservoirs is provided.

Keywords: microscopic remaining oil; pore-scale; micro-CT; flow rate; porosity

Citation: Liu, Y.; Pi, J.; Tong, K. Pore-Scale Experimental Investigation of the Residual Oil Formation in Carbonate Sample from the Middle East. *Processes* **2023**, *11*, 2289. https://doi.org/10.3390/pr11082289

Academic Editors: Chao Zhang, Fansheng Huang and Tengfei Wang

Received: 20 June 2023
Revised: 20 July 2023
Accepted: 26 July 2023
Published: 30 July 2023

1. Introduction

Carbonate rock reservoirs are an important component of the world's oil and gas resources, accounting for 70% of global oil and gas reserves and 60% of total oil and gas production [1]. The Middle East is a major distribution area for carbonate oil and gas reservoirs, which are primarily made up of porous carbonate rocks [2]. Water channels form easily during the development process due to the presence of heterogeneity in the formation. Oil displacement efficiency can only achieve 30% to 50% of the original oil saturation when the water cut exceeds 90%. The distribution of residual oil after water flooding becomes more complicated due to the complex pore throat results of porous carbonate rocks. The distribution of micro residual oil at the pore scale can provide new insights for improving carbonate rock oil recovery.

Many studies on carbonate reservoirs have been conducted by previous researchers. Ehrlich developed devices to measure the relative permeability of carbonate rock to oil and water [3]. He discovered that the displacement impact of carbonate rock was substantially less than that of typical sandstone, which led to the initial investigation of carbonate rock displacement. Herrera used full-diameter core analysis to determine correlation coefficients for high-velocity flow in fractured and vuggy reservoirs, advancing quantitative studies on the flow properties of carbonate rocks [4]. Using a glass micro-model model, M. R. Rokhforouz investigated the impact of fracture parameters on displacement under various wettability circumstances. He discovered that the flow rate of water injected into the matrix is low when there are fractures and that the degree of water invasion of the fractures rises

with the length of the fractures. A certain quantity of oil phases is also present in the center and bottom of bigger cracks, and the amount of trapped oil rises with the breadth of the fracture, according to his observations [5]. With the advancement of technology, CT technology has been widely applied to the field of petroleum engineering [6–8]. Micro-CT on the submillimeter level can be used to determine the physical parameters of porous media and fluid transport, providing a new method for pore-scale mechanism study [9]. With the help of micro-CT, predecessors have studied the effects of reservoir factors in real rock systems on the distribution of micro residual oil, such as pore throat structure, reservoir heterogeneity, and wettability [10–14].

Permeability, pore structure, injection rate, injected fluid, and other parameters all influence the distribution of oil and water in pores. At present, some studies have combined CT scanning technology with the brine injection method to study the influences of different kinds of residual oil in carbonate rock on the main flow channels (micro-pores) of cores and the change in core properties [15–19]. Jing initially explored the residual oil morphology of carbonate cores at different PVs by micro-CT and also quantified the residual oil in different states. The results show that when the injection multiplier exceeds 20 PV, a large amount of residual oil is displaced [20]. Guo analyzed the pore structure of four samples through fractal dimensions. He quantified and classified microscopic residual oil into five categories. Studies have shown that in high permeability samples, large connected oil clusters are more likely to decompose into small fragments, and all distribution patterns coexist with low permeability and complex pore structures [21]. The higher the pore sweep efficiency, the lower the heterogeneity, and the leftover oil masses are mostly trapped as discontinuous phases [22]. Li found that the residual oil saturation of the oil-wet plug is 19.8% lower than that of the water-wet plug (25.2%), and the trapped oil tends to occupy the center of the larger pores in the water-wet plug, while it tends to occupy the pore angle and adhere to the pore wall in the oil-wet plug [23]. However, due to technical limitations, micron-CT can only identify fluid in pores at the micron level. Through mercury intrusion testing on porous carbonate rocks, there is a large number of micro-pores. As an important percolation channel for porous carbonate rocks, the influence of micro-pores on the distribution of micro residual oil has been ignored in previous studies. Lin used differential imaging micro-tomography to identify micro-pores in carbonate rocks, providing information on additional conductivity between macro-cores via micro-porosity [24]. However, the effect of micro-porous properties on the microscopic residual oil distribution was not investigated in this study.

With the advancement of technology, the research methods of carbonate rock pore structure and water-flooding remaining oil are constantly innovating. Due to the complex pore type, pore structure, and rock fabric of carbonate reservoirs, the heterogeneity is extremely strong, so predecessors divided rocks into four categories according to the relative percentages of particles and mud: Mudstone, Wackstone, Packstone, and Grainstone [6]. Fang et al. explored the rock pore structure of carbonate reservoirs in the Middle East by using cast thin sections and established an identification model for rock pore throat types [7]. Tian et al. combined high-pressure mercury intrusion, scanning electron microscopy, and other methods to obtain the full-scale micro-pore size distribution curve of tight cores [8]. Sadefhnejad et al. proposed a new hybrid algorithm to reconstruct bimodal porous media by combining pore network modeling methods with image-based network techniques [9]. Krakowska, P. et al. confirmed petrophysical and flow properties and characterized the microstructure of porous rocks using 3D images generated by X-ray micro-computed tomography (micro-CT) [10]. These methods are helpful to study the physical properties of carbonate reservoirs, but the flow properties of carbonate rocks with complex pores after water flooding are still lacking. Scanning electron microscopy, mercury intrusion, casting thin sections, and other methods cannot carry out water flooding-related experiments, while CT scanning methods in the laboratory can determine the physical properties and fluid distribution of micron-scale porous media [7,25–28].

In this work, we use differential imaging micro-tography to identify micropores in porous carbonate rocks and investigate the effect of different micropore ratios on the microscopic residual oil distribution at different injection rates. In this paper, we use the 3 μm CT technology. The prepared core is put into the core gripper for scanning. Due to the limitation of the core size and the limitation of the accuracy of the scanning instrument, there are pores lower than 3 μm that cannot be recognized by the CT during the scanning process, and thus we use the super-resolution algorithm to process the scanned pictures.

In addition, the calculation method of oil saturation in micro-pores is further derived on the basis of the calculation method of micro-pores. Based on the above method, this study was conducted to explore: (1) Differences between macro-pores and micro-pores in porous carbonate rocks. (2) Effect of flow rate on oil saturation and morphology of remaining oil. (3) Variation of microporous residual oil saturation.

2. Materials and Methods

2.1. Rock Samples and Fluid

The rock sample is from the carbonate oil field in Iraq, with a diameter of 8 mm and a length of 50 mm. See Table 1 for the physical parameters of the sample. The macro-porosity and total micro-porosity of the CT scan are less than that of helium, indicating that some micro-porosity is not captured. The experimental fluid is No. 5 white oil and 30% KI aqueous solution, in which the KI solution is used to increase the contrast of the oil-water gray value and extract micro-pores in carbonate rock cores. The interfacial tension between oil and water is 0.074 n/m, and the viscosity and density of oil at room temperature and pressure are 4.638 mpa·s and 819.8 kg/m^3, respectively.

Table 1. Main petrophysical properties of the cores used in this study.

Core Number	Reservoir Type	Wettability	Permeability/mD	Helium Porosity/%
No. 1	Low permeability	Water-wet	6.00	4.55
No. 2	High permeability	Water-wet	311.9	26.35

2.2. Experimental Procedure

The micro-CT scanner is the nanovoxel-3502e series of Tianjin Sanying Precision Instrument Co., Ltd. (No. 28, Siwei Road, Dongli District, Tianjin, China). The in situ core-flooding experiments were carried out under identical flow conditions. The schematic diagram of the experimental device is shown in Figure 1. In the experiment, a carbon fiber core holder with constant temperature and pressure was employed. Samples were studied using a nano-focus tube at a voltage of 150 kV and current strength of 120 mA. The resolution of the survey for all samples was 3 μm. The plug was perpendicular to the horizontal plane in the micro-CT scanner, with the bottom as the fluid inlet and the top as the fluid outlet. The imaged region (field of view) was situated in the center of the sample, 25 mm above the bottom of the plug, to prevent the effects of end capillary pressure. The FOV is approximately 5.76 mm, 5.76 mm, and 4.608 mm. Each X-ray scan took about 130 min to acquire data. For all the tests presented in this paper, the pump is shut down to stop the fluid injection and maintain the initial constant temperature and pressure during the image acquisition stages.

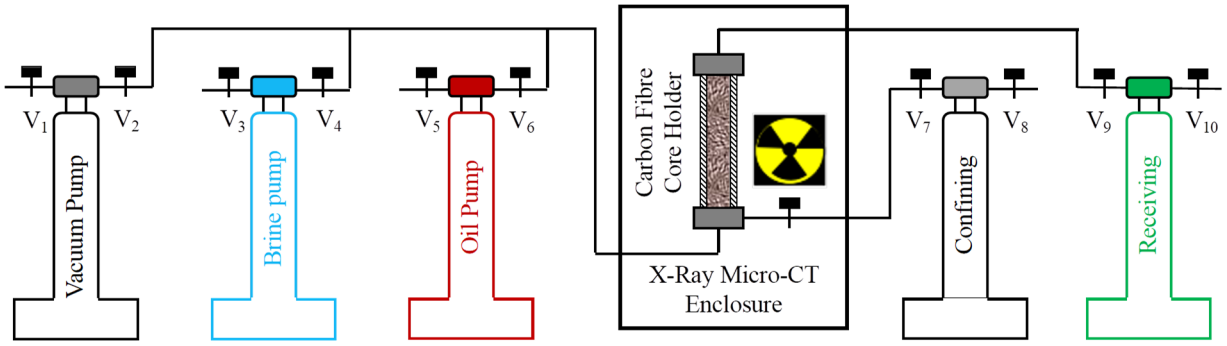

Figure 1. Schematic diagram of experimental device.

In situ scanning was performed throughout the experiment without changing the core holder; this was referred to as 4D X-ray tomography in certain reports [29,30]. The core-flooding experiment steps contain brine flooding and oil flooding. The specific experimental steps are as follows:

(1) The dry clean core plug was placed in the holder. The plug temperature and confining pressure were kept at 45 °C and 12 MPa, respectively, and stabilized for 5 h by using the back-pressure pump. The first micro-CT scan was performed on the dry plug. The dry scan was used for accurately mapping the pore space and generating porosity distribution along the field of views.

(2) The core plug was vacuumed and was then flooded with 100 pore volume (PV) of brine at a constant injection rate of 0.02 mL/min. It was let to stand for 12 h to ensure that the core was fully saturated with brine before oil injection. This approach can make a chemical equilibrium between rock minerals and brine. The micro-CT scan of the same locations was performed twice.

(3) Then, 100 PV of oil was injected through the core plug to establish a lower S_{wi}. The core plug was flushed with the mineral oil for a total of 100 PV at 0.02 mL/min and the 3D tomograms were recorded at the same locations. The oil flooding takes more than 100 h, which can reduce the effect of flowing oil on slow.

(4) Then, 20 PV at 0.02 mL/min of brine was injected through the core plug. The fourth micro-CT scan of the same locations was performed.

(5) A total of 20 PV of brine was injected at the higher flow rate of 0.05 mL/min and the fifth CT scan at the same locations was conducted.

(6) A total of 20 PV of brine was injected at the higher flow rate of 0.1 mL/min and the sixth CT scan at the same locations was conducted.

(7) Finally, the core plug was flooded with 20 PV of brine at the flow rate of 0.5 mL/min to establish a residual oil state. The seventh micro-CT scan of the same locations was performed.

2.3. Image Processing

Zeiss' proprietary software was used to recreate the tomograms. ImageJ and Avizo Fire 8.0 were used for all image processing. The slices were all horizontal cross-sections of the plug. As shown in Figure 2a, the tomogram was generated from the dry plug and then preprocessed to remove distorted exterior portions and external walls before being filtered with a nonlocal means edge-preserving filter [31]. This is because it is difficult to produce sufficient contrast between the solid and labeled fluids (mainly brine) in photos obtained from a flooded core [32]. By thresholding the dry plug image and using it as a mask for the wet photos, we created a pore map (Figure 2b).

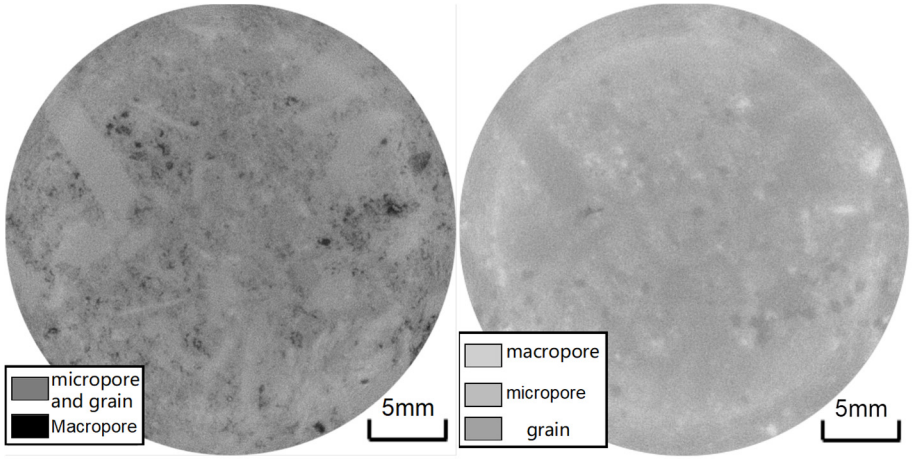

Figure 2. Horizontal cross-sectional slices through the core. (**a**) filtered dry reference image; (**b**) pore map obtained from the filtered dry image, where the pore is transparent and the grain is black.

However, micro-porosity can not be identified because carbonate rocks are prone to micropores and because scanning accuracy (3 μm) is limited. The differential imaging method is used to identify micro-pores. Figure 3a,b are cross-sectional views of dry samples and samples saturated with 30 wt.% KI salt water, respectively. Using high-concentration KI salt water can make the aqueous phase have a strong X-ray absorption capacity and make the water-bearing area brighter. It can be seen that the solid particles are saturated after using KI brine. The solid particle area with micro-pores is gray due to the existence of KI brine. The dry scanning image is subtracted from the saturated salt water scanning image to obtain different images, in which the black area is the rock skeleton, the white area is the micropore, and the gray area is the micro-pore, which makes the micro-pore area easier to distinguish (Figure 3c).

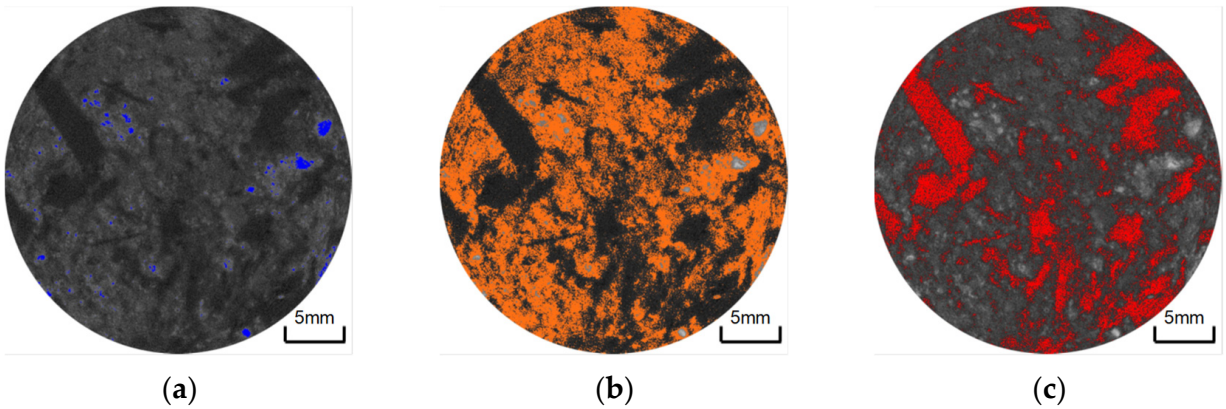

Figure 3. Horizontal cross-sectional slices through the core (diameter 5.76 mm) and the image processing workflow of wet and dry images taken during the oil-wet core-flooding experiment (slice number 5.76, 25.55 mm from the inlet). (**a**) Macro-pores are blue of Core 1; (**b**) micro-pores are yellow of Core 1; (**c**) grain is red.

The method of distinguishing the solid macro-pores and micro-pores is different from the previous. The method used in this paper is to extract the macro-pores using the watershed algorithm on the dry scanning image. The macro-pores part of the mask was removed from the differential image, and the watershed algorithm method was used again to distinguish the solid grains and micro-pores in the remaining part. The *CT* gray values distribution map of the three phases was obtained from the dry scanning image, and the peak values of the three phases were taken as the *CT* gray values of solid grains, macro-

pores, and micro-pores to calculate the porosity of the micro-pores (Figure 4), calculated as follows:

$$CT_{\text{micro}}^{dry} = CT_{\text{grain}} \times (1 - \phi_{\text{micro}}) + CT_{\text{macro}}^{dry} \times \phi_{\text{micro}}, \quad (1)$$

$$\phi_{\text{micro}} = \frac{CT_{\text{micro}}^{dry} - CT_{\text{grain}}}{CT_{\text{macro}}^{dry} - CT_{\text{grain}}} \quad (2)$$

where CT_{grain} is the CT gray value of the rock skeleton, CT_{micro}^{dry} and CT_{macro}^{dry} are the micro-phase CT gray value and macro-hole CT gray value relative to the dry scanning core. ϕ_{micro} is the porosity of micro-pores.

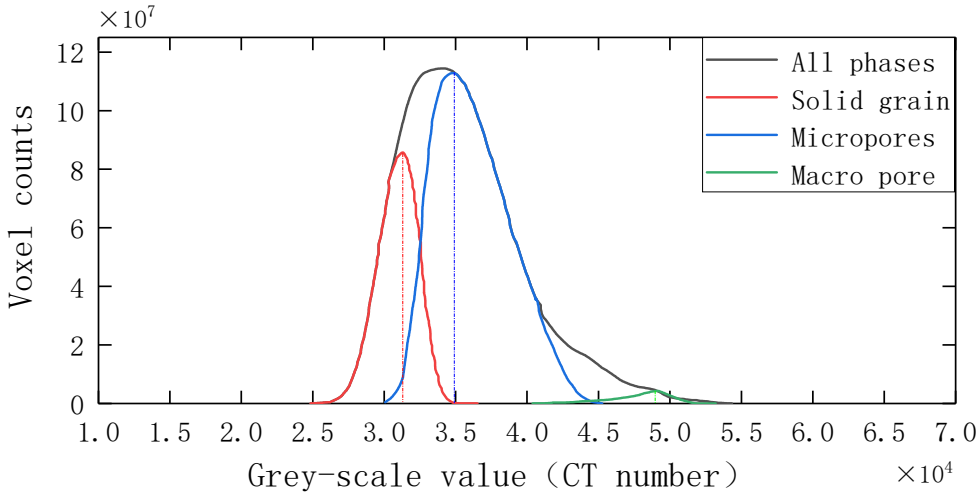

Figure 4. Histogram of different stages after image segmentation.

After the porosity of the micro-pores was obtained, the initial oil saturation of the micro-pores was obtained by adding the image of the saturated oil state. The oil-water distribution map in the saturated oil state was obtained by using the macro-pores as a mask. The above method was used to calculate the CT gray value of the oil phase, the water phase, and the micro-pores in the saturated oil image after the oil and water phases were segmented by using the watershed algorithm. The oil saturation of the micro-pores in different flow rates can be obtained by changing images under the corresponding states, calculated as follows:

$$CT_{\text{micro}}^{\text{oil}} = CT_{\text{grain}} \times (1 - \phi_{\text{micro}}) + CT_{\text{brine}} \times \phi_{\text{micro}} \times (1 - S_{O\_\text{micro}}) + CT_{\text{oil}} \times \phi_{\text{micro}} \times S_{O\_\text{micro}} \quad (3)$$

$$S_{o\_\text{micro}} = \frac{CT_{\text{micro}}^{\text{oil}} - CT_{\text{grain}} \times (1 - \phi_{\text{micro}}) - CT_{\text{brine}} \times \phi_{\text{micro}}}{CT_{\text{oil}} \times \phi_{\text{micro}} - CT_{\text{brine}} \times \phi_{\text{micro}}} \quad (4)$$

$CT_{\text{micro}}^{\text{oil}}$ is the CT gray value of micro-pores in the scanning image under saturated oil state, CT_{brine} and CT_{oil} are the CT gray value of 30% KI water phase and oil phase, respectively, and S_{o_micro} is the oil saturation of micro-pores [33].

The above method can only extract the part of the micro-pores based on the existing image resolution but cannot accurately divide the fluid components in the micro-pores. In this paper, the author used the above methods combined with the super-resolution image enhancement method to improve the original image. The resolution divides the micropore range to determine the pore throat and remaining oil distribution.

The classification basis is mainly through the training of high-precision core section pictures, and the SRCNN method is used to improve the accuracy of the core. Selected core sections are shown in Figure 5.

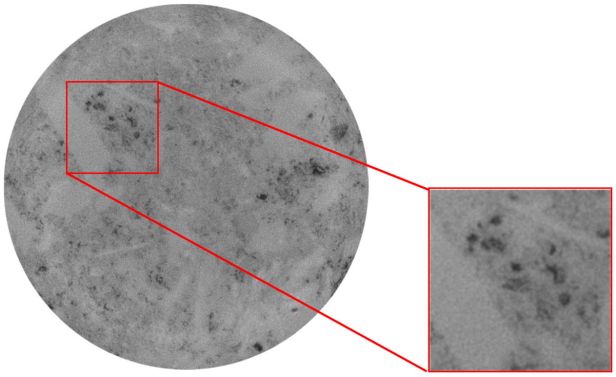

Figure 5. The slice of Core 1.

A higher-resolution image was obtained by microscopic electron microscopy scanning of core No. 2. The high-resolution images were trained. A 500 × 500 slice of CT scan of core No. 2 was selected and the original image was super-resolved, as shown in Figure 6.

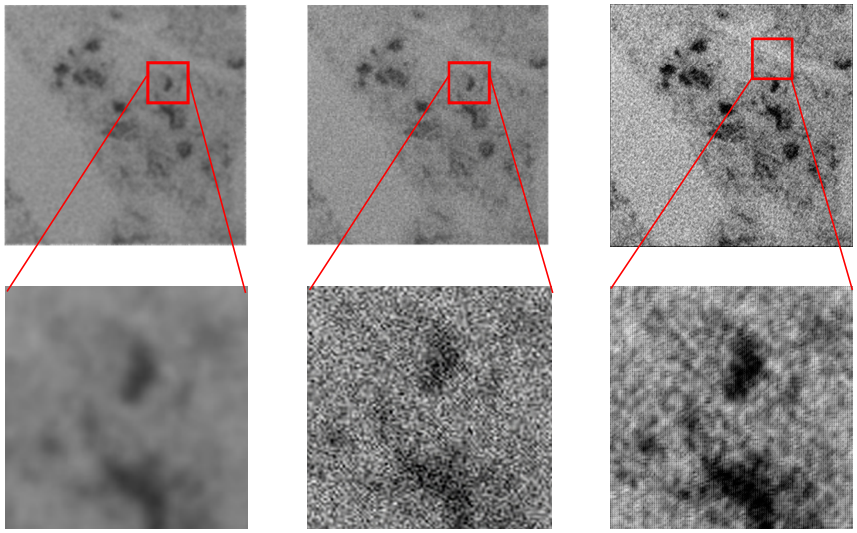

(**a**) Original image (**b**) 2× Super-resolution (**c**) 4× Super-resolution

Figure 6. Comparison of different reconstruction multipliers.

This paper compares super-resolution convolutional neural networks, super-resolution adversarial neural networks, and self-supervised learning algorithms, comparing the peak signal-to-noise ratios and the image clarity evaluation functions of the different methods at different resolutions in Table 2, respectively, in order to determine the super-resolution algorithm used in this paper as the optimal method.

Table 2. Number of hole throats in No. 2 core.

Reconstruction Methods	Reconstruction Ratio	Peak Signal-to-Noise Ratio	SMD
SRCNN	2	6.23	8.34
	4	22.67	16.25
SRGAN	2	2.77	3.16
	4	18.23	10.23
DBPI	2	4.56	3.13
	4	20.12	12.35

2.3.1. Peak Signal-to-Noise Ratio

The peak signal-to-noise ratio mainly reflects the error between the corresponding pixel points of two images of the same size. The higher the value represents the closer

the reconstructed image is to the original image, and thus the higher the quality of the reconstructed image. The formula is as follows:

$$PSNR = 10 \times \log_{10}\left(\frac{MAX_I^2}{MSE}\right)$$

where MSE denotes the mean square error in the two images and is calculated as follows:

$$MSE = \frac{1}{H \times W \times C}\|\hat{X} - X\|_2^2$$

MAX_I indicates the maximum value of an image pixel point.

2.3.2. Image Sharpness Evaluation Function

SMD evaluates the sharpness of an image by calculating the sum of the absolute values of the differences between neighboring pixels within the image.

The larger the value of *SMD*, the clearer the image. Its calculation formula is as follows:

$$SMD = \sum_i \sum_j [|I(i,j) - I(i,j-1)| + |I(i,j) - I(i+1,j)|]$$

where $I(i,j)$ indicates the size of the gray value of the corresponding coordinate pixel.

By extracting the internal feature information of the image after super-resolution processing, the missing details in the magnified image are compensated, and the image resolution and contrast are improved at the same time. The sub-resolution pores inside the carbonate rock that could not be identified in the original image are captured. The differences between the three images are compared in Figure 6. The pores that could not be distinguished in the original image are reflected in the 2× super-resolution image, while the 4× super-resolution image shows more pores that cannot be distinguished in the original image. There is no significant increase in noise. It is proved that the 4× super-resolution image processing can ensure both the improvement of the image resolution and the stability of the image.

3. Results and Discussion

3.1. Representative Elementary Volume

The larger the amount of data, the more likely the image will show the characteristics of the core, but the computing power of the computer may not be able to calculate the experimental core results as a whole. Therefore, in order to meet the computing power of the computer, we need to select the characterization unit of the core for computer image processing, that is, the smallest core unit that can effectively characterize the physical properties of the core, that is, the physical properties obtained by studying the smallest unit are the same as those of the whole core. Taking porosity and saturation as parameters and segmented data volume as the research object, a series of three-dimensional data cubes with different side lengths are intercepted, and the macro-porosity and micro-porosity of each data volume are calculated, respectively. The calculation results show that with the increase in the data volume, each curve gradually tends to be horizontal, indicating that the scanning field of view is larger than the characterization unit volume of the core, and the study area can represent the whole core.

The data blocks with different lengths are sheared, and the macro-porosity and micro-porosity of each cube are obtained. The length of the cube ranges from 50 pixels (150 μm) to 1500 pixels. As shown in Figure 7, with the increase in the amount of data, when the length of the scanned cube is greater than 500 pixels, the change of each parameter curve gradually tends to be horizontal. Therefore, it is determined that the basic volume of the research object is a cube with a side length of 500 pixels.

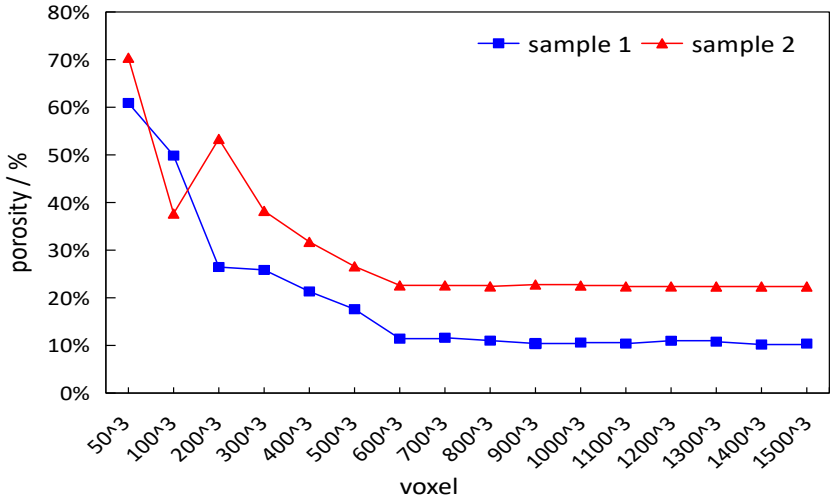

Figure 7. Representative elementary volume.

3.2. Microscopic Pore Structure

After determining the characterization unit body, the pore throats in the unit body are extracted, as shown in the following Figures 8 and 9.

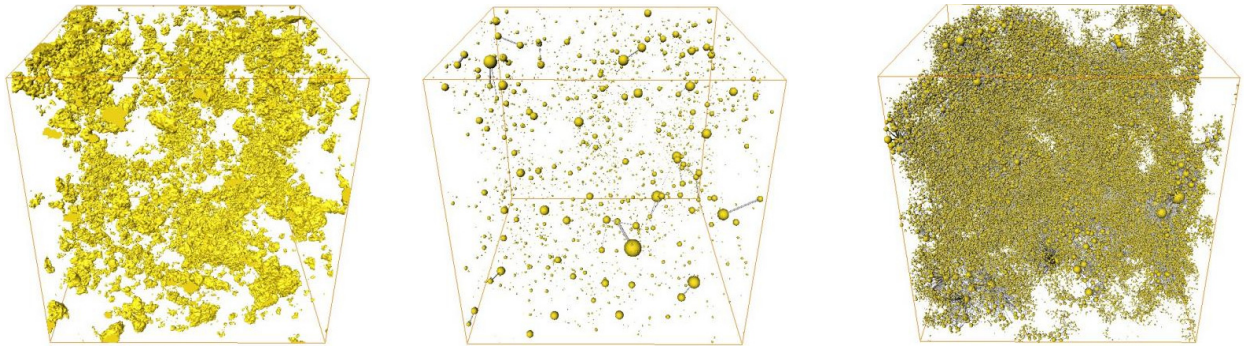

(**a**) (**b**) (**c**)

Figure 8. Pore network model of Sample 1. (**a**) Pore space can be identified; (**b**) Pore throat network model before processing; (**c**) Pore throat network model after processing.

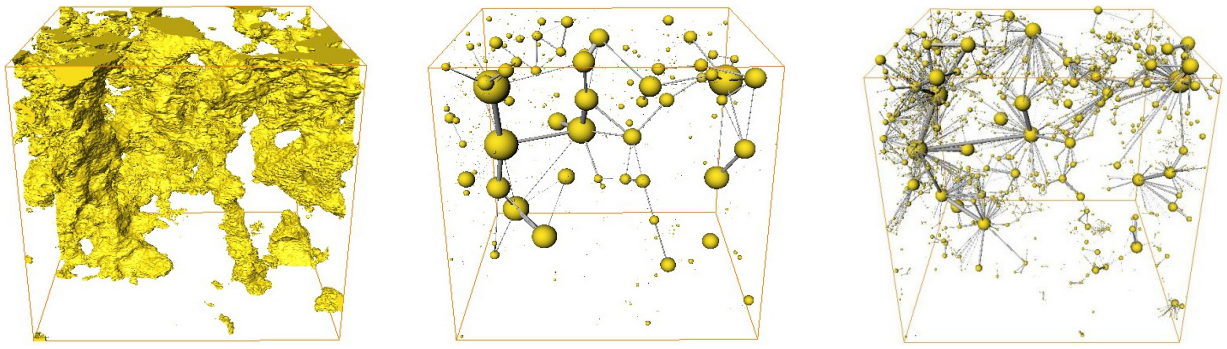

(**a**) (**b**) (**c**)

Figure 9. Pore network model of Sample 2. (**a**) Pore space can be identified; (**b**) Pore throat network model before processing; (**c**) Pore throat network model after processing.

By simulating the pore network of the extracted pores, taking Sample 1 as an example to compare the pore-throat network model before and after processing, combined with the distribution frequency and coordination number, it can be found that there are many micropores in the core that cannot be directly identified by CT scanning. Pores with a radius

of less than 1.5 µm and throats with a radius of less than 0.8 µm could not be identified before processing, while pores and throats with higher precision could be identified after processing. Figure 10 compares the frequency of pore throat distribution before and after treatment. A comparison of the number of pore-throat identifications before and after processing the two samples is shown in Table 3. It can be found that the number of pore identifications in the Sample 1 image after processing is 47.88 times higher than that of the untreated pore identification number, and the number of throats is increased by 10,443.38 times. The number of identifications is increased by 9.09 times, and the number of throat identifications is increased by 92.79 times.

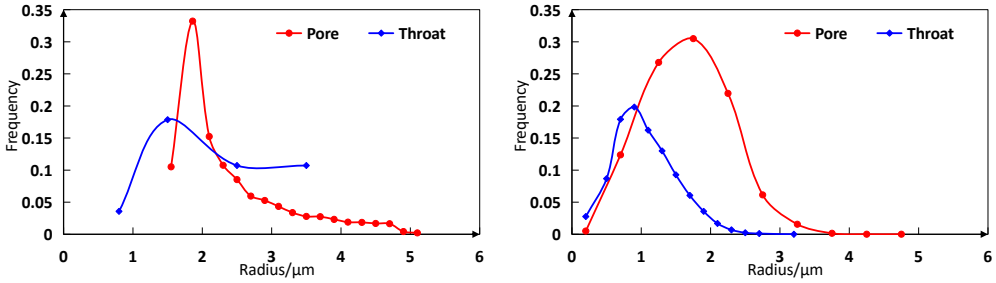

(**a**) Before processing (**b**) After processing

Figure 10. Relationship between pore throat radius and frequency before and after treatment of Sample 1.

Table 3. Comparison of the number of pore throats.

	Sample 1		**Sample 2**	
	Pore	Throat	Pore	Throat
Before treatment	1397	34	237	56
After treatment	2899	1402	2154	5196
Effect	47.88	10,443.38	9.09	92.79

As shown in Figure 11, the coordination number of the two samples before treatment is mainly 0, which means that many pores are in an independent state and are not connected, but after treatment, it can be found that most of the pore throats are in a connected state. Combined with the number and distribution of pore throats, it shows that there are many pores and throats in the actual core that cannot be directly identified by CT, and there are a large number of sub-resolution pore throats in low-permeability samples as connecting channels for oil-water migration.

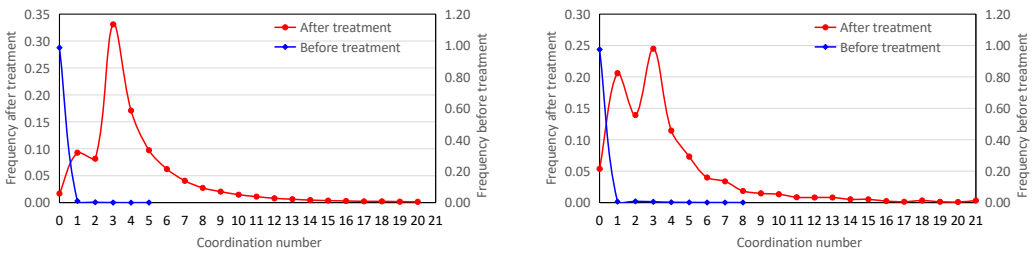

(**a**) Sample 1 (**b**) Sample 2

Figure 11. Coordination number.

We calculated the micro- and macro-porosity (Figure 12). The porosity in Core 1's slice numbers 2–40, 98–172 was high, but the overall distribution was relatively uniform from the slice map of porosity. The extreme difference in porosity between slices is 6.50%. After identifying the micro-pores, the extreme difference in micro-pore porosity is 3.70% and the extreme difference in macro-pore porosity is 5.55%. The porosity in Core 2's slice

numbers 0–150, 200–315, and 350–446 was high, and the overall distribution was relatively not uniform from the slice map of porosity. The extreme difference in porosity between slices is 28.69%. After identifying the micro-pores, the extreme difference in micro-pore porosity is 2.39% and the extreme difference in macro-pore porosity is 28.29%. The results indicate that micro-pores have a greater impact on Core 1, while macro-pores have a greater impact on Core 2. It is proved that the cores with more micro-pores have poorer physical properties, while the cores with more macro-pores have better physical properties. It can be seen from the figure below that Core 1 has more contribution from micro-pores and Core 2 has more contribution from macro-pores.

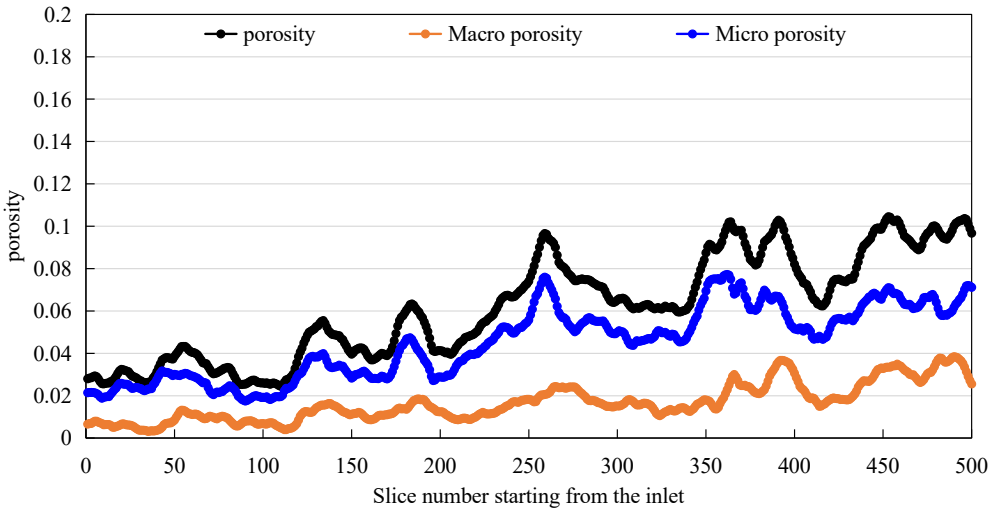

(**a**) Core 1

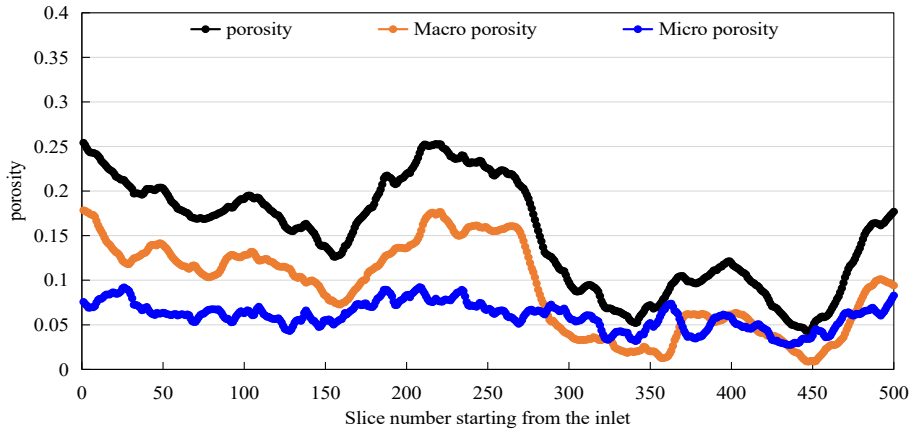

(**b**) Core 2

Figure 12. Macro/micro/total porosity of core under 2D slice.

3.3. Variation Characteristics of Remaining Oil Distribution in Sub-Resolution Pore Throats

The oil phase in the core scanning image is extracted, and the oil saturation in the two stages before and after the initial saturated oil state of the Sample 1 core is calculated (see Figures 13 and 14).

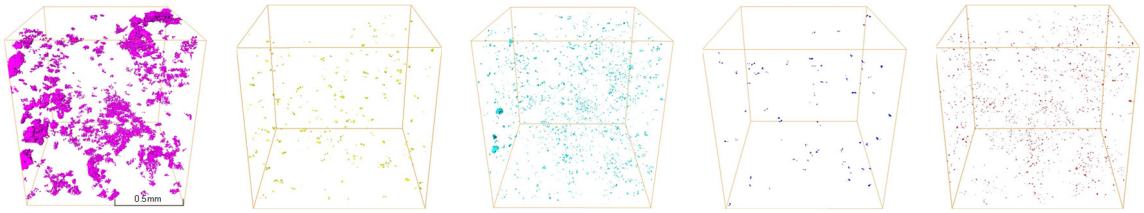

(**a**) Cluster (**b**) Porous (**c**) Membranous (**d**) Columnar (**e**) Dropwise

Figure 13. Distribution of remaining oil in original core of Sample 1 in saturated oil state.

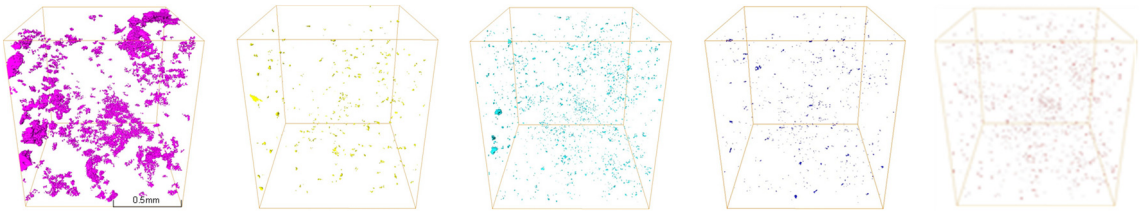

(**a**) Cluster (**b**) Porous (**c**) Membranous (**d**) Columnar (**e**) Dropwise

Figure 14. Distribution of remaining oil in core oil-saturated state after Sample 1 treatment.

After determining the pore network, the frequency corresponding to different oil content of each pore throat is calculated, the oil content characteristics of two different displacement stages before and after two cores are compared, and the size of sub-resolution pores based on the CT number in saturated water state is determined. The oil content is determined according to the gray value. When the oil content is high, the water phase is expelled, and the area is determined as the area with higher oil saturation, that is, the area with a lower CT number. When the oil content is low, that is, the water phase is not expelled or the pore throat is small and the water content is small, it is determined as the area with low oil saturation, that is, the area with a high CT number.

As shown in Figure 13, the oil-bearing areas in the saturated oil state and the two states after displacement of 20 PV were selected and the remaining oil within the radius of 0.001–1 μm below the resolution was selected. It can be seen that with the continuous water flooding, the main sub-resolution displacement, the frequency of the remaining oil within 0.001–0.01 μm decreases, while the frequency of remaining oil within 0.01–0.1 μm increases, indicating that the remaining oil in the sub-resolution pore throats is mainly used for small pore throats during the displacement process. The remaining oil inside is expelled.

3.4. Morphology of Oil Cluster in Macro-Pores

A detached oil ganglion can be isolated and quantitatively characterized using topological morphology analysis of leftover oil based on the form factor, Euler number, and contact ratio. Table 4 shows the computation formula and physical meaning of the shape factor, Euler number, and contact ratio. According to the five flow regimes, the remaining oil can be categorized from hard-to-produce to easy-to-produce. Membranous flow, droplet flow, columnar flow, multi-porous flow, and clustered flow are all examples of it [34]. The exploitation method for multi-porous flow and clustered flow is to increase microscopic sweep efficiency, such as polymer flooding or polymer microsphere displacement. In general, the exploitation method for membranous flow, droplet flow, and columnar flow increases the microscopic displacement efficiency, such as surfactant flooding.

Table 4. Calculation formula and physical meaning of the characterization parameters.

Characterization Parameter	Calculation Formula	Physical Meaning
Shape Factor	$\text{Shape Factor} = \frac{\text{Surface Area}^3}{36\pi \times \text{Volume}^2}$	The degree of similarity between the shape of a single piece of leftover oil and spheres. The value of the sphere is one, and the smaller the value, the closer the form is to a sphere, and the greater, the more irregular the shape
Euler Number	$\text{Euler Number} = 1 - \text{conectivity} + \text{enclosed cavities}$	Reflect the pore number of single piece of remaining oil number. The smaller the value, the more the pore holes.
Contact Ratio	$\text{Contact Ratio} = \frac{\text{Contact Area Between Oil and Rock}}{\text{Surface Area of Oill}}$	Provide the contact relationship between single piece of remaining oil and the hole wall. The smaller the contact ratio, the less the remaining oil adhering to pore surface.

As shown in Figure 15. Comparing the proportions of the remaining oils of the five types before and after treatment, it was found that the proportions of cluster, porous, film, and residual oils decreased, while the proportions of columnar and droplet residual oils increased. Since the recognition accuracy of the processed images for small pore throats is improved, more residual oil in the pore throats can be identified, and the residual oil in the form of droplets is easily adsorbed in the small pore throats, so the proportion of residual oil in the form of droplets increases. By identifying more fine pore throats, a lot of remaining oil in a connected state that has not been identified before can be found, but the number of connected adjacent pore throats is less than five, which belongs to porous residual oil, so the proportion of porous residual oil increases.

By extracting the oil phase of the processed images under different PVs, the change process of the distribution of various types of remaining oil during the water flooding process was calculated and observed.

In the low-permeability core, with the gradual increase in the displacement ratio, the proportion of the remaining oil in clusters decreases, and the proportions of remaining oil in droplets and columns first decrease and then increase, indicating that during the whole displacement process, the proportion of remaining oil in clusters and the drop-shaped and column-shaped residual oil is preferentially displaced at the beginning of the displacement, and the cluster-shaped residual oil mainly occurs in the large pore throats and is displaced by the pressure difference. In the pore throat, displacement is carried out by capillary force. It shows that the sub-resolution micro-pores are the main communication channels for oil-water migration during the entire displacement process of the low-permeability samples.

In high permeability cores, with the increase in the displacement multiple, the proportion of continuous remaining oil is decreasing, and the proportion of discontinuous remaining oil is increasing, indicating that during the displacement process, the continuous remaining oil is mainly displaced, the pore throats above the resolution in the core are mainly the oil-water seepage channel, and the pressure difference is the main source of displacement.

The remaining oil classification for macro-pores is shown in Table 3. It shows the classification of the microscopic remaining oil in the two states using the classification method in Section 3.4. The flow was found to decrease gradually with an increasing flooding rate while the discontinuous phase increased.

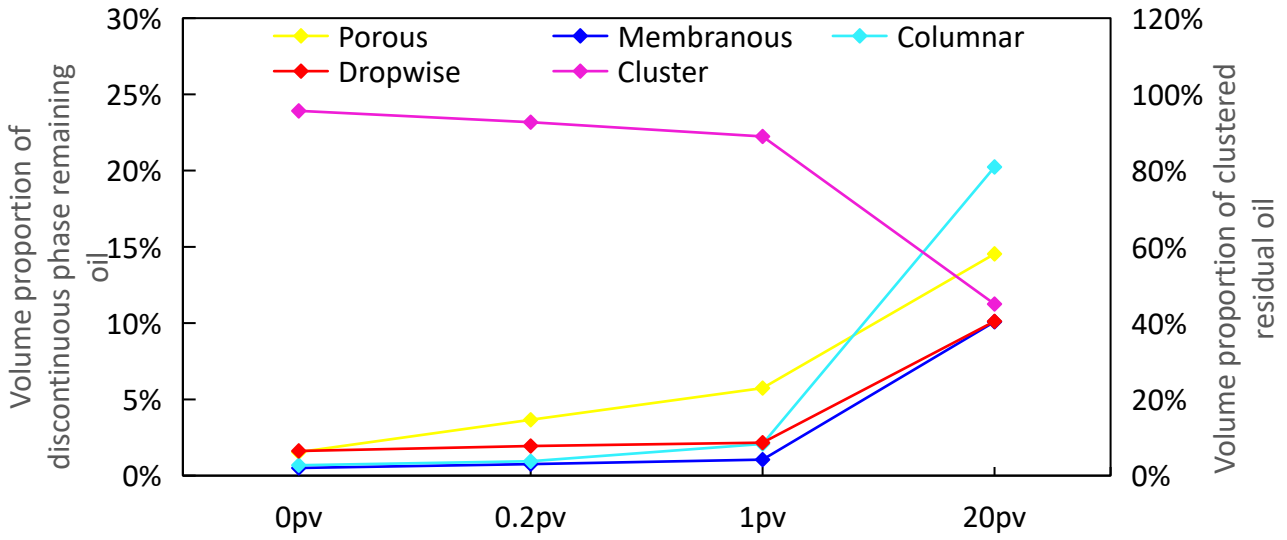

(**a**) Sample 1

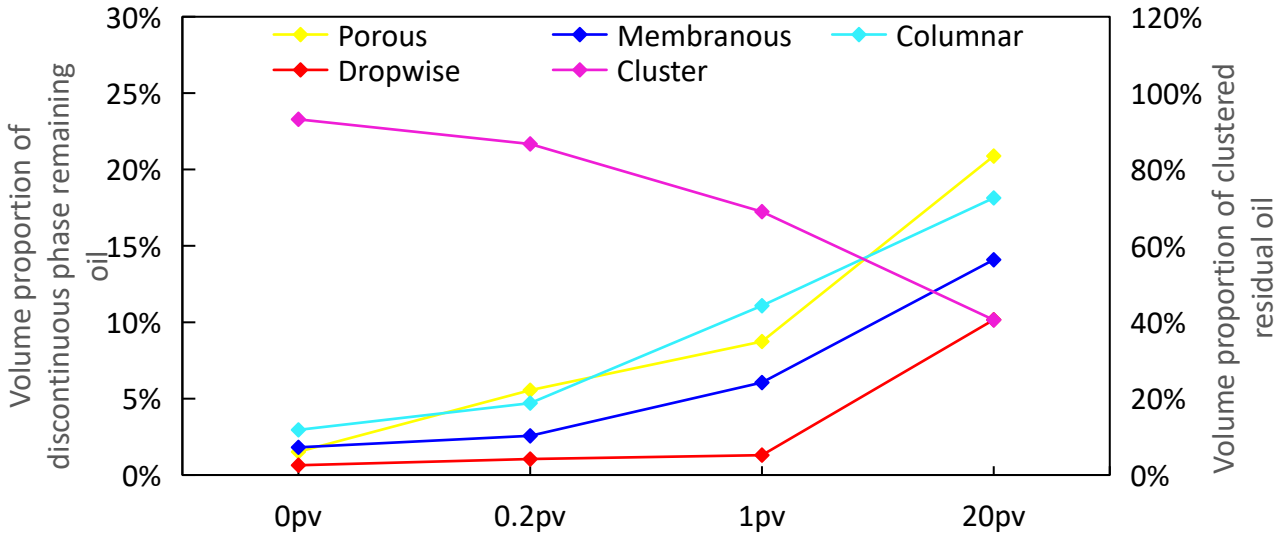

(**b**) Sample 2

Figure 15. Distribution of various types of remaining oil under different displacement degrees.

As shown in Figure 16, the oil-bearing areas in the saturated oil state and the two states after displacement of 20 PV were selected and the remaining oil within the radius of 0.001–1 μm below the resolution was selected. It can be seen that with the continuous water flooding, in sub-resolution displacement, the frequency of the remaining oil within 0.001–0.01 μm decreases, while the frequency of remaining oil within 0.01–0.1 μm increases, indicating that the remaining oil in the sub-resolution pore throats is mainly used for small pore throats during the displacement process. The remaining oil inside is expelled.

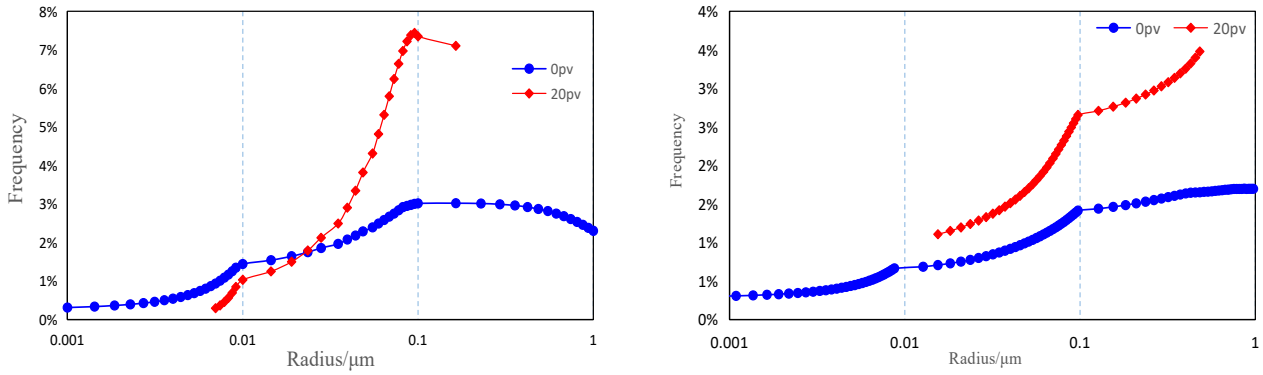

(**a**) Sample 1 (**b**) Sample 2

Figure 16. Pore throat radius and frequency.

Further statistics on the volume ratio of the two kinds of microscopic remaining oil in different states can be found in Figure 9. As a result of the above discussion, the continuous phase was gradually broken up into discontinuous phases as the flow rate increased.

With the increase in rate, the cluster flow decomposition efficiency of Core 1 was the highest when the flow rate was higher than 0.1 mL/min. The cluster flow decomposition efficiency of Core 2 was highest when the flow rate was higher than 0.02 mL/min. The results show that Core 1 requires a higher flow rate than Core 2 to effectively replace the cluster flow.

By extracting the oil phase in the core scanning image, we can clearly observe the change process of different types of remaining oil in the process of water flooding. The final remaining oil saturation of the two cores after flooding at different flow rates is shown in Table 5.

Table 5. Final residual oil saturation.

	Core 1	**Core 2**
0.02 mL/min	49.34%	56.11%
0.5 mL/min	36.25%	46.32%

In the process of water flooding, the continuous oil phase in the core pores is gradually divided by the water phase to form isolated oil clusters (drops), and the separation speed and the number of oil clusters (drops) are closely related to the displacement speed and core physical properties.

3.4.1. Effect of PV on Remaining Oil

As is shown in Figure 17, with the increase in flooding rate, the remaining oil saturation of the core continues to decrease. In the oil-saturated state, it can be found that most of the oil clusters are continuous, and a small part of the discontinuous phase remaining oil is dispersed throughout the core. With the increase in displacement rate, the proportion of clustered residual oil in residual oil continues to decline, and the residual oil of the discontinuous phase, such as film and drop, continues to increase. After 0.5 mL/min rate flooding, the continuous oil phase is broken up into the discontinuous phase to the greatest extent. In the later stage, the remaining oil is mainly clustered, but the film and drop account for more than 25%. The experimental results show that the high-rate water flooding breaks up the continuous phase oil cluster into the discontinuous phase, which is conducive to the discharge of the remaining oil in the continuous phase. However, it will produce discontinuous phase remaining oil, which is not easily discharged.

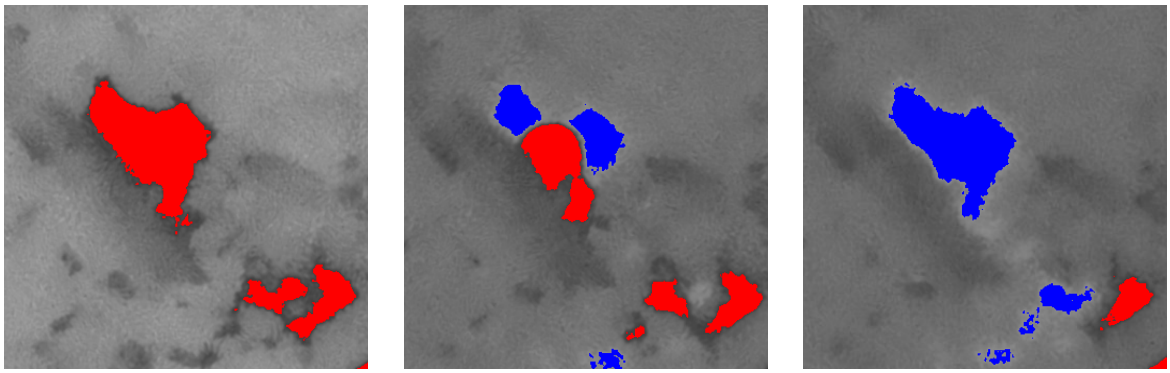

(**a**) (**b**) (**c**)

Figure 17. Horizontal cross-sectional slices of Core 2. (**a**) Oil saturated state; (**b**) 0.1 PV; (**c**) 20 PV, where oil and brine are red and blue, respectively.

3.4.2. Influence of Micropore

The higher percentage of micro-pores cores require a higher flooding rate and pressure to flood the same proportion of residual oil as high permeability residual oil. However, a low percentage of micro-pore cores are less prone to cluster residual oil being dispersed into discontinuous residual oil. The lower percentage of micro-pore cores of Core 2 is higher than that of Core 1, and the subsequent crude oil recovery is the highest. It can be seen that macro-porosity, permeability, and flooding rate affect the migration of the oil phase and the distribution of remaining oil in the core to varying degrees.

3.5. Variation of Residual Oil Saturation in Micro-Pores

In this section, we first calculate the micro oil saturation of each interval based on the data volume of CT scanning. Then, its occurrence state and distribution are analyzed, and the micro residual oil at different flow rates is calculated. Finally, the effects of different flow rates on micro residual oil are discussed.

Through the slice results, it can be found that the total porosity of the core in Core 1 is mainly micro-pores, and the total porosity of the core in Core 2 is mainly macro-pores, indicating that the proportion of micro-pores in the overall core in low-permeability carbonate rocks controls the basic permeability of the core. Micro-facies porosity is shown in Table 6.

Table 6. Micro-facies porosity.

	Core 1			Core 2		
Type	**Volume Fraction**	**Pore Contribution Rate**	**Contribution to Total Porosity**	**Volume Fraction**	**Pore Contribution Rate**	**Contribution to Total Porosity**
Rock skeleton	0.377	0	0	0.582	0	0
Micro-porous phase region	0.552	0.130	0.072	0.408	0.176	0.072
Macro-pore area	0.071	1	0.071	0.011	1	0.011
Overall porosity		0.143			0.083	

Table 6 shows the pore composition of the two core characterization units. Core 1 has high porosity and low permeability. The physical properties are dominated by micro-pores, 90.38% of total core porosity in micro-pores. Core 2 has high porosity and high permeability, with the physical properties of the core dominated by macro-pores. Micro-pore porosity accounts for 21.84% of total core porosity.

4. Conclusions

(1) Micro-pores govern the porosity of high-porosity and low-permeability carbonate reservoirs, while macro-pores control the porosity of high and high-permeability carbonate reservoirs;
(2) The leftover oil in the micro-pores is initially displaced during brine flooding of carbonate reservoirs. When some of the remaining oil in the micro-pore is displaced, the micro-pores become connected to the macro-pores, and the remaining oil in the macro-pores is displaced;
(3) The remaining oil in the micro-pores is preferentially displaced as the flow rate increases, and the capillary force is used as the displacement force. When the micro-pores link to the macro-pores, much of the remaining oil in the macro-pores is moved;
(4) The image enhancement method improves the identification effect of the carbonate core's pore throat. The recognition effect of Sample 1′s pore throat is 47.88 times and 10,443.38 times greater than before treatment; Sample 2′s recognition effect is 9.09 times and 92.76 times greater than before treatment. This method's effect is clearly superior to that of hypertonic samples in hypotonic samples;
(5) The remaining oil content gradually diminishes as displacement velocity increases. When a particular speed is reached, the influence of continual displacement speed improvement on the total remaining oil is lessened.

Author Contributions: Conceptualization, Y.L., J.P. and K.T.; investigation, Y.L.; methodology, Y.L.; writing—original draft, Y.L.; writing—review and editing, J.P. and K.T.; investigation, K.T. All authors have read and agreed to the published version of the manuscript.

Funding: This research received no external funding.

Data Availability Statement: Not applicable.

Conflicts of Interest: The authors declare no conflict of interest.

References

1. Zhang, N.N.; He, D.F.; Sun, Y.P.; Li, H. Global distribution characteristics of large oil and gas fields in carbonate rocks and their controlling factors. *China Pet. Explor.* **2014**, *19*, 54–65.
2. Liu, H.Y.; Tian, C.Y.; Guo, R.; Yi, L. Status and prospects of research on rock classification methods for complex carbonate reservoirs. *Adv. Geophys.* **2017**, *32*, 2057–2064.
3. Ehrlich, R. Relative Permeability Characteristics of Vugular Cores-Their Measurement and Sinificance. In Proceedings of the Society of Fall Meeting of the Petroleum Engineers of AIME, New Orleans, LA, USA, 3–6 October 1971.
4. Herrera, R.G.; Fernando, S.V.; Hernandez, F.P. On the Petrophysics of Carbonate Reservoirsthrough Whole Cole Analysis. In Proceedings of the International Petroleum Conference and Exhibition, Veracruz, Mexico, 10–13 October 1994; Volume 10, pp. 10–13.
5. Rokhforouz, M.; Amiri, H.A. Pore-level influence of micro-fracture parameters on visco-capillary behavior of two-phase displacements in porous media. *Adv. Water Resour.* **2018**, *113*, 260–271. [CrossRef]
6. Liu, X.; Wang, J.; Ge, L.; Hu, F.; Li, C.; Li, X.; Yu, J.; Xu, H.; Lu, S.; Xue, Q. Pore-Scale Characterization of Tight Sandstone inYanchang Formation Ordos Basin China Using Micro-CT and SEM Imaging from Nm- to Cm-Scale. *Fuel* **2017**, *209*, 254–264. [CrossRef]
7. Iglauer, S.; Fernø, M.; Shearing, P.; Blunt, M. Comparison of Residual Oil Cluster Size Distribution, Morphology and Saturation in Oil-Wet and Water-Wet Sandstone. *J. Colloid Interface Sci.* **2012**, *375*, 187–192. [CrossRef] [PubMed]
8. Liu, B.; Ma, R.; Fan, H. Evaluation of the Impact of Freeze-Thaw Cycles on Pore Structure Characteristics of Black Soil Using X-Ray Computed Tomography. *Soil Tillage Res.* **2021**, *206*, 104810. [CrossRef]
9. She, Y.; Zhang, C.; Mahardika, M.A.; Patmonoaji, A.; Hu, Y.; Matsushita, S.; Suekane, T. Pore-Scale Study of in-Situ Surfactant Flooding with Strong Oil Emulsification in Sandstone Based on X-Ray Microtomography. *J. Ind. Eng. Chem.* **2021**, *98*, 247–261. [CrossRef]
10. Knackstedt, M.A.; Arns, C.H.; Ghous, A.; Sakellariou, A.; Senden, T.J.; Sheppard, A.P.; Sok, R.M.; Nguyen, V.; Pinczewsk, W.V. 3D imaging and characterization of the pore space of carbonate core; implications to single and two phase flow properties. In Proceedings of the SPWLA 47th Annual Logging Symposium, Veracruz, Mexico, 4–7 June 2006.
11. Armstrong, R.T.; Wildenschild, D.; Bay, B.K. The effect of pore morphology on microbial enhanced oil recovery. *J. Pet. Sci. Eng.* **2015**, *130*, 16–25. [CrossRef]

12. Okazaki, K.; Michibayashi, K.; Hatakeyama, K.; Abe, N.; Johnson, K.T.M.; Kelemen, P.B.; The Oman Drilling Project Science Team. Major mineral fraction and physical properties of carbonated peridotite (listvenite) from ICDP Oman drilling project hole BT1B inferred from X-ray CT core images. *J. Geophys. Res.* **2021**, *126*, e2021JB022719. [CrossRef]
13. Alyafei, N.; Raeini, A.; Paluszny, A.; Blunt, M. A sensitivity study of the effect of image resolution on predicted petrophysical properties. *Transp. Porous Media* **2015**, *110*, 157–169. [CrossRef]
14. Bazaikin, Y.; Gurevich, B.; Iglauer, S.; Khachkova, T.; Kolyukhin, D.; Lebedev, M.; Lisitsa, V.; Reshetova, G. Effect of CTimage size and resolution on the accuracy of rock property estimates. *J. Geophys. Res.* **2017**, *122*, 3635–3647. [CrossRef]
15. Han, J.; Han, S.; Kang, D.H.; Kim, Y.; Lee, J.; Lee, Y. Application of digital rock physics using X-ray CT for study on alteration of macropore properties by CO_2 EOR in a carbonate oil reservoir. *J. Pet. Sci. Eng.* **2020**, *189*, 107009. [CrossRef]
16. Zhang, H.; Chen, G.; Zhu, Y.; Dang, Y.; Chen, J.; Wang, H.; Si, Y.; Bai, C.; Li, X. Quantitative characterization of microscopic pore throat structure in tight sandstone oil reservoirs: A case study of Chang7 reservoir in Xin'anbian oil field, Ordos Basin. *Pet. Geol. Exp.* **2017**, *39*, 112–119.
17. Yin, D.; Zhang, X. Study on Micro Pore Structure Characteristics of Yangdachengzi Oil Layer in Chaoyanggou Oilfield. *J. Petrochem. Univ.* **2021**, *34*, 39–45.
18. Zhang, T.; Sun, S. Thermodynamics-Informed Neural Network (TINN) for Phase Equilibrium Calculations Considering Capillary Pressure. *Energies* **2021**, *14*, 7724. [CrossRef]
19. Zhang, T.; Sun, S. A coupled Lattice Boltzmann approach to simulate gas flow and transport in shale reservoirs with dynamic sorption. *Fuel* **2019**, *246*, 196–203. [CrossRef]
20. Jing, W.; Zhang, L.; Li, A.; Yang, Y.; Zhong, J.; Sun, H.; Yao, J. Investigation of Pore-Scale Remaining Oil Dynamic Evolution in Heterogeneous Marine Carbonate Using Real-Time Computed Tomography Scanning. *Energy Fuels* **2022**, *36*, 8180–8188. [CrossRef]
21. Guo, C.; Wang, X.; Wang, H.; He, S.; Liu, H.; Zhu, P. Effect of Pore Structure on Displacement Efficiency and Oil-Cluster Morphology by Using Micro Computed Tomography (MCT) Technique. *Fuel* **2018**, *230*, 430–439. [CrossRef]
22. Li, J.; Liu, Y.; Gao, Y.; Cheng, B.; Meng, F.; Xu, H. Effects of Microscopic Pore Structure Heterogeneity on the Distribution and Morphology of Remaining Oil. *Pet. Explor. Dev.* **2018**, *45*, 1112–1122. [CrossRef]
23. Li, J.; Gao, Y.; Jiang, H.; Liu, Y.; Dong, H. Pore-Scale Imaging of the Oil Cluster Dynamic during Drainage and Imbibition Using in Situ X-Ray Microtomography. *Geofluids* **2018**, *2018*, 7679607. [CrossRef]
24. Lin, Q.; Al-Khulaifi, Y.; Blunt, M.J.; Bijeljic, B. Quantification of Sub-Resolution Porosity in Carbonate Rocks by Applying High-Salinity Contrast Brine Using X-Ray Microtomography Differential Imaging. *Adv. Water Resour.* **2016**, *96*, 306–322. [CrossRef]
25. Iglauer, S.; Paluszny, A.; Blunt, M.J. Simultaneous oil recovery and residual gas storage: A pore-level analysis using in situ X-ray micro-tomography. *Fuel* **2013**, *103*, 905–914. [CrossRef]
26. Iglauer, S.; Rahman, T.; Sarmadivaleh, M.; Al-Hinai, A.; Fernø, M.A.; Lebedev, M. Influence of wettability on residual gas trapping and enhanced oil recovery in three-phase flow: A pore-scale analysis by use of microcomputed tomography. *SPE J.* **2016**, *21*, 1916–1929. [CrossRef]
27. Andrew, M.; Bijeljic, B.; Blunt, M.J. Pore-scale imaging of geological carbon dioxide storage under in situ conditions. *Geophys. Res. Lett.* **2013**, *40*, 3915–3918. [CrossRef]
28. Andrew, M.; Bijeljic, B.; Blunt, M.J. Pore-by-pore capillary pressure measurements using X-ray microtomography at reservoir conditions: Curvature, snap-off, and remobilization of residual CO_2. *Water Resour. Res.* **2015**, *50*, 8760–8774. [CrossRef]
29. Mustafin, A.Z.; Li, K.; Varfolomeev, M.A.; Yuan, C.; Kadyrov, R.I.; Glukhov, M.S.; Khayrtdinov, R.K.; Pu, W.; Sattarov, A.I.; Statsenko, E.O. A case study of salt-tolerant functional polymer for EOR in carbonate reservoirs with ultra-high salinity. In Proceedings of the SPE Russian Petroleum Technology Conference, Virtual, 26–29 October 2020.
30. Panahi, H.; Kobchenko, M.; Renard, F.; Mazzini, A.; Scheibert, J.; Dysthe, D.; Jamtveit, B.; Malthe-Sorenssen, A.; Meakin, P. A 4D synchrotron X-raytomography study of the formation of hydrocarbon- migration pathways in heated organic-rich shale. *SPE J.* **2013**, *18*, 366–377. [CrossRef]
31. Buades, A.; Coll, B.; Morel, J.M. A non-local algorithm for image denoising. In Proceedings of the 2005 IEEE Computer Society Conference on Computer Vision and Pattern Recognition, San Diego, CA, USA, 20–25 June 2005; Volume 2, pp. 60–65.
32. Khishvand, M.; Akarabadi, M.; Piri, M. Micro-scale experimental investigation of the effect of flow rate on trapping in sandstone and carbonate rock samples. *Adv. Water Resour.* **2016**, *94*, 379–399. [CrossRef]
33. Cheng, B.; Li, J.; Jiang, S.; Lu, C.; Su, H.; Yu, F.; Jiang, H. Pore-Scale Investigation of Microscopic Remaining Oil Variation Characteristic in Different Flow Rates Using Micro-CT. *Energies* **2021**, *14*, 3057. [CrossRef]
34. Li, J.; Jiang, H.; Wang, C.; Zhao, Y.; Gao, Y.; Pei, Y.; Wang, C.; Dong, H. Pore-scale investigation of microscopic remaining oil variation characteristics in water-wet sandstone using CT scanning. *J. Nat. Gas Sci. Eng.* **2017**, *48*, 36–45. [CrossRef]